

See discussions, stats, and author profiles for this publication at: <https://www.researchgate.net/publication/231650040>

Structural Characterization and Catalytic Activity of Nanosized $Ce_xM_{1-x}O_2$ (M = Zr and Hf) Mixed Oxides

ARTICLE in THE JOURNAL OF PHYSICAL CHEMISTRY C · JULY 2008

Impact Factor: 4.77 · DOI: 10.1021/jp802674m

CITATIONS

65

READS

29

3 AUTHORS:



Benjaram M Reddy

CSIR-Indian Institute of Chemical Technolo...

280 PUBLICATIONS **5,703** CITATIONS

SEE PROFILE



Pankaj Bharali

Tezpur University

38 PUBLICATIONS **621** CITATIONS

SEE PROFILE



Pranjal Saikia

Gauhati University

30 PUBLICATIONS **441** CITATIONS

SEE PROFILE

Structural Characterization and Catalytic Activity of Nanosized $\text{Ce}_x\text{M}_{1-x}\text{O}_2$ ($\text{M} = \text{Zr}$ and Hf) Mixed Oxides

Benjaram M. Reddy,* Pankaj Bharali, and Pranjal Saikia

Inorganic and Physical Chemistry Division, Indian Institute of Chemical Technology, Hyderabad-500 607, India

Sang-Eon Park

Laboratory of Nano-Green Catalysis, Department of Chemistry, Inha University, Incheon 402-751, Republic of Korea

Maurits W. E. van den Berg, Martin Muhler, and Wolfgang Grünert

Lehrstuhl für Technische Chemie, Ruhr-Universität Bochum, D-44780 Bochum, Germany

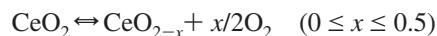
Received: March 27, 2008; Revised Manuscript Received: May 19, 2008

A systematic study was conducted to understand the influence of two different dopant cations (Zr^{4+} and Hf^{4+}) incorporated into the ceria lattice. A modified coprecipitation technique was employed to make the investigated $\text{Ce}_x\text{Zr}_{1-x}\text{O}_2$ (CZ) and $\text{Ce}_x\text{Hf}_{1-x}\text{O}_2$ (CH) mixed oxides. The study was comprised of extensive characterization of the prepared catalysts using different techniques, namely, X-ray powder diffraction (XRD), Raman spectroscopy (RS), X-ray photoelectron spectroscopy (XPS), ion scattering spectroscopy (ISS), transmission electron microscopy (TEM), UV–vis diffuse reflectance spectroscopy (UV–vis DRS), and BET surface area method. To assess the usefulness of these catalysts, oxygen storage–release capacity (OSC) and CO oxidation activity measurements were performed. The XRD analyses reveal that the CZ sample bears $\text{Ce}_{0.75}\text{Zr}_{0.25}\text{O}_2$ and $\text{Ce}_{0.6}\text{Zr}_{0.4}\text{O}_2$ phases and the CH sample possesses only the $\text{Ce}_{0.8}\text{Hf}_{0.2}\text{O}_2$ phase after calcination at different temperatures (773–1073 K). RS measurements suggest a defective structure of the mixed oxides resulting in the formation of oxygen vacancies. The TEM results indicate nanometer-sized crystallites and there is no appreciable increase in the particle size even after high temperature treatments. The XPS studies reveal the presence of cerium in both Ce^{3+} and Ce^{4+} oxidation states. The ISS results indicate surface enrichment of cerium in the case of the CH sample, while such surface enrichment of cerium is not observed for the CZ sample. The UV–vis DRS measurements provide information about $\text{Ce}^{4+} \leftarrow \text{O}^{2-}$ and $\text{Ce}^{3+} \leftarrow \text{O}^{2-}$ charge transfer transitions. The absence of free ZrO_2 and HfO_2 in the mixed oxides tenders the clue about the formation of respective solid solutions. The CH catalyst exhibited better OSC and CO oxidation activity compared to that of the CZ sample. The OSC and CO oxidation activity results correlate well with the structural characterization data. The influence of ionic radii of dopant cations on the overall performance of the ceria-based mixed oxides is contemplated.

Introduction

Ceria (CeO_2) has attracted considerable interest in recent years due to its diverse applications. It is a candidate material for a wide variety of applications ranging from catalysis to ceramic biomaterials, fuel cell technologies, electrochemical applications, optical glass-polishing, gas sensors, and so on. Although disagreements remain about the mechanism that ceria plays in many of these applications, it is clear that redox properties of ceria or doped ceria or ceria solid solutions are very important.^{1–5} Owing to the facile redox couple ($\text{Ce}^{4+}/\text{Ce}^{3+}$) and elevated oxygen ion migration ability, it has been used for years as one of the components of catalytic automobile exhaust converters. Catalytic converters, which convert the three primary pollutants in automobile exhaust-gas, namely, CO, NO_x , and hydrocarbons, into nontoxic products are referred to as three-way catalysts (TWC). Improvements in such features are currently in demand for designing better catalytic cartridges for new-generation

cleaner cars.⁶ The conversion efficiency of TWC is highly dependent upon the air-to-fuel (A/F) ratio, which has to be maintained at the stoichiometric level (~ 14.6).⁷ To maintain this level the catalyst must possess oxygen storage capacity (OSC) so that it can provide oxygen to the gas mixture during fuel-rich conditions and absorb oxygen in fuel-lean conditions. Hence, the redox chemistry of ceria is a critical parameter in the efficiency of the multifunctional and multicomponent three-way catalysts.⁸ The release and uptake of oxygen in ceria occurs owing to the following reversible reaction.⁹



However, for direct automotive applications, the OSC and thermal durability of pure ceria are insufficient.^{10,11} Also, it is an established fact that ceria exhibits a cubic fluorite structure and sinters equally three dimensionally. Therefore, many studies have been carried out in this direction to increase the thermal stability and the OSC of ceria.^{12–15}

The mixed metal oxides have played an important role recently in many areas of chemistry, physics, material science,

* Corresponding author. E-mail: bmreddy@iict.res.in or mreddyb@yahoo.com.

and geochemistry. Obviously, the chemical behavior of mixed metal oxides may differ from that of single metal oxides. The combination of two metal oxides in an oxide matrix can lead to novel structural and electronic properties of the final oxide, favoring its catalytic activity. At structural levels, a dopant can facilitate defect formation within the oxide host by generating stress into the lattice. On the contrary, nontypical coordination modes of lattice host resulting in a deviation in the dopant's chemical nature may also be possible. As a result, metal–metal or metal–oxygen–metal interactions in mixed metal oxides lead to perturbed electronic states compared to single metal oxides. Although most of the recent literature concerning alternative materials for TWC applications deals with ceria–zirconia based systems, the redox properties and chemical activity of pure ceria can be enhanced by introducing different types of metals (Ca, Cu, Tb, Mn, etc.) into the oxide lattice other than zirconium.^{16–18} However, it is not clear what type of second metal is useful to improve both the stability at high temperature and the chemical activity by introducing O vacancies in the ceria. For example, Zr mixing improved the thermal stability of ceria nanoparticles but showed no significant O vacancies, whereas Ca mixing introduced a lot of O vacancies in the host structure, but the mixed metal oxide bears a relatively low stability and phase segregation into CeO₂ and CaO occurs at temperatures close to 973 K.^{19,20} Therefore, it was interesting to investigate the effect of substitution of a new dopant with a smaller ionic radius than zirconium into the ceria lattice.

It is already realized in heterogeneous catalysis that catalytic activity scales with surface area. Hence, maximum dispersion of the particles is of extraordinary importance, which makes the production of nanoscaled catalysts very tempting. The nanoparticle configurations are interesting from a practical viewpoint also as most of the applications are surface-sensitive, and a high surface-to-volume ratio in addition to improved redox properties, related to oxygen vacancy generation, can be reached by using nanosized materials. In a recent communication, we have demonstrated the efficiency of Hf⁴⁺ (ionic radius 0.78 Å) on the OSC and CO oxidation activity of ceria when incorporated even in smaller quantities than Zr⁴⁺ (ionic radius 0.84 Å).²¹ Against this background, an extensive characterization of the ceria–hafnia solid solution was carried out and presented here. Given the importance of ceria and particularly of ceria–zirconia solid solutions, and further to help resolve some of the apparent discrepancies between the Ce–Hf and Ce–Zr mixed oxides, a reference ceria–zirconia solid solution was also examined for comparison purposes.

Experimental Procedures

Catalyst Preparation. The Ce_xHf_{1-x}O₂ (80:20 mol % based on oxides; CH) and Ce_xZr_{1-x}O₂ (50:50 mol % based on oxides; CZ) mixed oxides were prepared by adopting a coprecipitation method. These catalysts were prepared in a 20 g batch. In a typical procedure, to synthesize the CH sample, a 0.44 M solution was prepared by dissolving 48.8 g of ammonium cerium(IV) nitrate (Loba Chemie, GR grade) in 200 mL of deionized water and a 0.11 M solution was prepared by dissolving 7.1 g of hafnium(IV) chloride (Aldrich, AR grade) in 200 mL of deionized water separately and then the two solutions were mixed together. In a similar way to make the CZ sample, a 0.34 M solution was prepared by dissolving 37.2 g of ammonium cerium(IV) nitrate (Loba Chemie, GR grade) in 200 mL of deionized water and a 0.34 M solution was prepared by dissolving 29.1 g of zirconium(IV) nitrate (Fluka, AR grade) in 200 mL of deionized water separately and then the two

solutions were mixed together. Then the mixed solutions were stirred for another 1 h under mild stirring conditions. The mixed solutions were then diluted to 4000 mL with deionized water and stirred for 3 h. Upon complete dissolution, dilute aqueous ammonia (25% NH₃ solution) was added dropwise with vigorous stirring until the precipitation was complete (pH ~8.5). The complete process of precipitating the mixed-metal hydroxides was performed over 5 h. The resulting slurry was filtered off by using Whatmann filter paper under mild vacuum and thoroughly washed with 2000 mL of deionized water to remove the anion impurities. The accumulated mixed oxide pastes were carefully placed in a clean ceramic crucible, which was covered, and allowed to dry overnight in a hood. The resulting samples were then oven-dried at 393 K for 12 h and finally calcined at 773 K for 5 h in dry air atmosphere at a gas flow rate of 20 mL min⁻¹ and a heating rate of 5 deg min⁻¹ to remove water and any residual precursors remaining from the coprecipitation step. Some portions of the 773 K calcined samples were again thermally treated with the same experimental conditions as above at 873, 973, and 1073 K for 5 h to study the thermal stability of the catalyst systems. After cooling, the solid residue was ground by using a ceramic or glass mortar and pestle until a fine powder was obtained, which was then labeled and stored in glass vials.

Catalyst Characterization. X-ray powder diffraction patterns were recorded on a Rigaku Multiflex instrument, using a nickel-filtered Cu Kα (0.15418 nm) radiation source and a scintillation counter detector. The XRD phases present in the samples were identified with the help of a Powder Diffraction File-International Center for Diffraction Data (PDF-ICDD). The average crystallite size of the oxide phases was estimated with the help of the Scherrer equation by using the XRD data of all prominent lines, and the lattice parameter was calculated by a standard cubic indexation method, using the intensity of the most prominent peak (111). The Raman spectra were recorded with a LabRam HR spectrometer (Jobin Yvon) equipped with a charge-coupled device (CCD) detector. The emission line at 514.53 nm from an Ar⁺-Kr⁺ ion RM2018 laser (Spectra Physics) was focused on the sample under the microscope, with the diameter of the analyzed spot being ~1 μm. The power of the incident beam on the sample was typically 0.5 mW. The time of acquisition was adjusted according to the intensity of the Raman scattering. The wavenumber values reported from the spectra are accurate to within 1 cm⁻¹. To ascertain the homogeneity of the samples, spectra were recorded at various points and compared. All samples were found to be highly homogeneous. The TEM images were obtained on a JEM-2010 (JEOL) instrument equipped with a slow-scan CCD camera and at an accelerating voltage of 200 kV. Samples were sonically dispersed in ethanol and deposited on a carbon-coated copper grid before examination. The BET surface areas were determined by N₂ physisorption at liquid N₂ temperature on a Micromeritics Gemini 2360 instrument. Prior to analysis, the samples were oven-dried at 393 K for 12 h and flushed with Argon gas for 2 h.

The XPS measurements were made on a Shimadzu (ESCA 3400) spectrometer by using Mg Kα (1253.6 eV) radiation as the excitation source. Charging of catalyst samples was corrected by setting the binding energy (BE) maximum of the C 1s peak envelope corresponding to carbon atoms bonded to other carbon and hydrogen atoms to be at 284.6 eV. The finely ground oven-dried samples were dusted on a double stick graphite sheet and mounted on the standard sample holder. The sample holder was transferred to the analysis chamber through a rod attached to

TABLE 1: BET Surface Area, XRD Phases, Crystallite Size, Lattice Parameter, and Oxygen Storage Capacity Measurements of Ce_xHf_{1-x}O₂ (CH) and Ce_xZr_{1-x}O₂ (CZ) Samples Calcined at Different Temperatures

sample	calcination temp (K)	S.A. (m ² g ⁻¹)	XRD phases	size ^a (nm)	“ <i>a</i> ” ^b (Å)	OSC (δ) ^c
CH	773	78	Ce _{0.8} Hf _{0.2} O ₂	4.6	5.34	0.19
	873	62	Ce _{0.8} Hf _{0.2} O ₂	6.3	5.34	
	973	40	Ce _{0.8} Hf _{0.2} O ₂	7.2	5.34	
	1073	26	Ce _{0.8} Hf _{0.2} O ₂	13.1	5.34	
CZ	773	84	Ce _{0.75} Zr _{0.25} O ₂	4.7	5.35	0.16
	873	67	Ce _{0.75} Zr _{0.25} O ₂	4.8	5.33	
	973	51	Ce _{0.75} Zr _{0.25} O ₂	5.0	5.30	0.12
	1073	36	Ce _{0.75} Zr _{0.25} O ₂ ; Ce _{0.6} Zr _{0.4} O ₂	5.5	5.27	

^a Crystallite size from the Scherrer equation. ^b Lattice parameter. ^c Oxygen vacancy concentration obtained in the second stage of heat treatment.

it. The XPS analysis was done at room temperature and pressures were typically in the order of less than 10⁻⁸ Pa. The samples were outgassed in a vacuum oven overnight before XPS measurements. The ion scattering spectroscopy (ISS) measurements were performed on a Leybold surface analysis system equipped with X-ray and ion sources, and an EA 10/100 electron (ion) analyzer with multichannel detection (Specs). The samples were pretreated in flowing synthetic air (20% O₂/N₂) at 573 K for 0.5 h before they were introduced into the spectrometer vacuum without further contact with the ambient humid atmosphere (in situ treatment). The measurements were done with 3000 eV Ar⁺ and 2500 eV Ne⁺ ions for CH and CZ samples, respectively, and recorded with the analyzer in pass-energy mode. The surface charge was removed with a flood gun. The source and the flood gun were allowed to stabilize with the sample withdrawn from the measurement position. Signal intensities were estimated assuming the background to be linear. The UV-vis DRS measurements were performed over the wavelength range 200–800 nm, using a GBS-Cintra 10e UV-vis NIR spectrophotometer with integration sphere diffuse reflectance attachment. Samples were diluted in a KBr matrix by pelletization.

OSC Measurements. The OSC was determined by the oxygen release characteristics of the samples in the temperature region 573–1073 K. The change in the weight of the sample was monitored by thermogravimetry (TG) under cyclic heat treatments in flowing nitrogen or dry air. A commercial Netzsch TG-DTA analyzer (Luxx, STA, 409 PC, Germany) was employed for this purpose. The heat cycle consisted of heating the sample to 1073 K, cooling to 423 K, and again heating to 1073 K. All heating and cooling rates were 5 deg min⁻¹. The weight loss of the sample during the second stage of heat treatment was used to measure the oxygen release properties.²²

CO Oxidation Activity. The catalytic activity of the synthesized nanosized mixed oxides was evaluated for oxidation of CO at normal atmospheric pressure and temperatures in the range of 300–773 K in a fixed bed microreactor at a heating ramp of 5 deg min⁻¹. About 100 mg of catalyst sample (250–355 μm sieve fraction) diluted with quartz particles of the same sieve fraction was placed in a quartz reactor for evaluation. Temperature was measured directly at the catalyst bed, using a thermocouple placed in the hollow shaft of the reactor. The following gases and gas mixtures were used (supplied by Air Liquide): argon (>99.999% purity), 9.98% CO in argon (CO purity, >99.997%; argon purity, >99.99%), and 10.2% O₂ in argon (oxygen purity, >99.995%). The total flow rates maintained by three mass flow controllers were in the range of 50–60 NmL min⁻¹ (milliliters normalized to 273.15 K and 1 atm.). The CO and CO₂ gas concentrations were measured

by using an Uras 14 infrared analyzer module, and the O₂ concentration was measured with a Magnos 16 analyzer (Hartmann & Braun). Prior to oxidation of CO, the catalysts were heated to 773 K in 10.2% O₂/Ar gas mixture, using a heating ramp of 10 deg min⁻¹, and kept at the final temperature for 1 h. The oxidized sample was then purged in argon and cooled to the desired starting temperature. The CO/O₂ reactant feed ratio was 1, and partial pressures of CO and O₂ were in the range of 10 mbar.

Results and Discussion

The N₂ BET surface area, crystallite size, cell "a" parameter, and OSC results pertaining to Ce_xHf_{1-x}O₂ (CH) and Ce_xZr_{1-x}O₂ (CZ) samples calcined at different temperatures are presented in Table 1. The BET results indicate reasonably high specific surface areas for both series of samples. The CH and CZ samples calcined at 773 K bear a specific surface area of 78 and 84 m² g⁻¹, respectively. Pure CeO₂ prepared by a similar method possessed a specific surface area of 41 m² g⁻¹.²³ This observation indicates that the incorporation of Hf⁴⁺ and Zr⁴⁺ into the ceria lattice induces an increase in the surface area. It is generally known that the mixed oxides with highest possible specific surface area are of great interest in view of their practical utility. However, for CeO₂, the stored oxygen comes mostly from the near-surface region, but for solid solutions of cerium-containing oxides oxygen comes from the bulk as well, owing to high oxygen diffusivity. Therefore, surface area is not the mere factor to determine the catalytic efficiency of ceria-based mixed oxides. As can be seen from Table 1, thermal treatments at higher temperatures cause gradual sintering and crystallite growth resulting in the loss of surface area. However, the resistance to thermal sintering of these mixed oxides is remarkable in comparison to that of pure ceria.²³

The XRD patterns of various samples calcined at 773–1073 K are presented in Figure 1. These results reveal the formation of solid solutions with typical cubic fluorite phases of the composition Ce_{0.8}Hf_{0.2}O₂ (PDF-ICDD 04-006-1933) and Ce_{0.75}Zr_{0.25}O₂ (PDF-ICDD 28-0271), respectively, for 773 K calcined samples. Upon increasing calcination temperature to 1073 K, the same monophasic composition is retained for the CH sample but phase segregation into Ce_{0.75}Zr_{0.25}O₂ and Ce_{0.6}Zr_{0.4}O₂ (PDF-ICDD 38-1439) was observed for the CZ sample. No XRD lines pertaining to either HfO₂ or ZrO₂ were observed in the respective cases. Also gradual sharpening of the XRD peaks with increasing calcination temperature could be observed as a result of the sintering phenomenon. The presence of a single-phase solid solution is always preferable compared to that of microdomain or phase-segregated nonho-

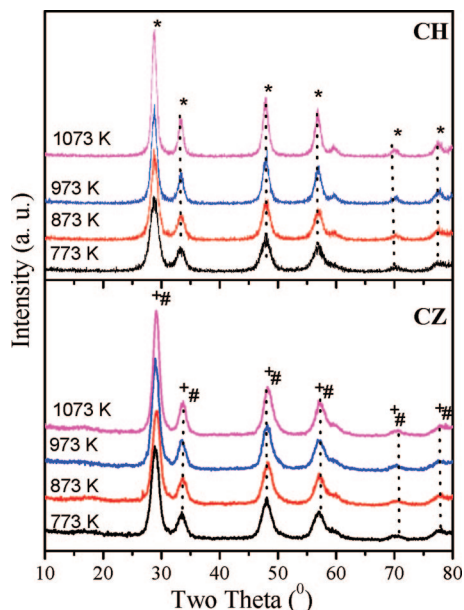


Figure 1. Powder XRD patterns of $\text{Ce}_x\text{Hf}_{1-x}\text{O}_2$ (CH) and $\text{Ce}_x\text{Zr}_{1-x}\text{O}_2$ (CZ) samples calcined at various temperatures. The peak legends are as follows: (*) $\text{Ce}_{0.8}\text{Hf}_{0.2}\text{O}_2$; (+) $\text{Ce}_{0.75}\text{Zr}_{0.25}\text{O}_2$; (#) $\text{Ce}_{0.6}\text{Zr}_{0.4}\text{O}_2$.

homogeneous mixed oxides, as the former systems generally lead to better textural stability and redox properties.^{24,25} XRD analysis reveals only the cubic phase and any departure from the internal cubic symmetry cannot be distinguished by using XRD due to the small atomic scattering factor of oxygen in comparison to those of Zr, Hf, and Ce, which dominate the diffractograms.^{26–28} It has been reported previously that ceria–zirconia solid solutions with intermediate compositions can form metastable tetragonal phases that are difficult to distinguish from a true cubic phase with use of XRD alone.²⁹ This might be the case for the present $\text{Ce}_x\text{Zr}_{1-x}\text{O}_2$ and $\text{Ce}_x\text{Hf}_{1-x}\text{O}_2$ mixed oxides, given that the widths of the diffraction peaks made it impossible to distinguish between cubic and tetragonal phases.⁵ Therefore, other techniques, particularly Raman spectral analysis, were used as complementary tools.

The crystallite sizes (D_{XRD}) calculated with the Scherrer equation are presented in Table 1. As shown in the table, mixed oxide particles of both samples are in the nanometer range. The 773 K calcined samples bear a crystallite size of ca. 5 nm, which increases slightly at higher calcination temperatures. There is a significant influence of Hf^{4+} and Zr^{4+} cations in the ceria lattice to decrease the particle sizes compared to that of pure CeO_2 .²³ The higher values of crystallite size of the mixed oxides after high temperature treatment are due to the effect of sintering.^{21,23} The lattice parameter calculations for both Hf^{4+} and Zr^{4+} incorporated ceria mixed oxides are presented in Table 1. The observed change in the cell “a” parameter values of all the samples indicates penetration of Hf^{4+} and Zr^{4+} cations into the ceria cubic lattice resulting in the formation of solid solutions. Relative to pure ceria (5.41 Å) the cell “a” parameter values of CH and CZ samples decreased to 5.34 and 5.35 Å, respectively, for the 773 K calcined samples.²¹ At higher calcination temperatures the cell parameter values decreased slightly for the CZ sample, while no such change was observed for the CH sample. This observation may be attributed to further shrinkage of ceria lattice due to the replacement of Ce^{4+} (0.97 Å) ions with smaller cations of Zr^{4+} (0.84 Å), caused by phase segregation of the Ce–Zr oxide phases, especially at higher temperatures. This fact has been elaborated in subsequent paragraphs.

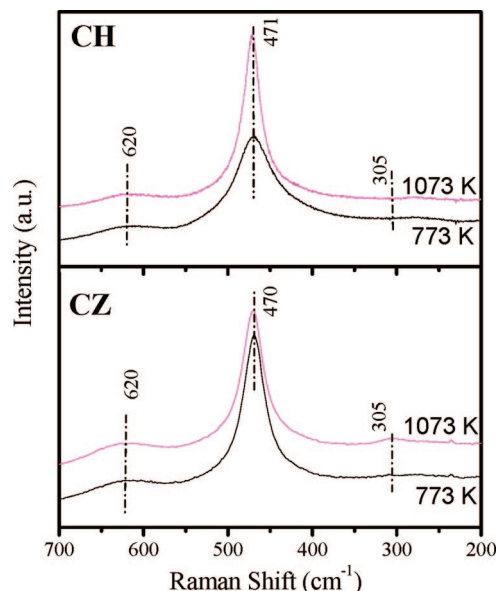


Figure 2. Raman spectra of $\text{Ce}_x\text{Hf}_{1-x}\text{O}_2$ (CH) and $\text{Ce}_x\text{Zr}_{1-x}\text{O}_2$ (CZ) samples calcined at various temperatures.

The Raman spectra of various samples calcined at 773 and 1073 K are shown in Figure 2. The Raman spectra of CH and CZ samples reveal a weak band at $\sim 305\text{ cm}^{-1}$ and a shoulder at $\sim 620\text{ cm}^{-1}$, in addition to the most intense peaks at 469/470 and 470/471 cm^{-1} , respectively. The most intense peaks are due to F_{2g} vibration of the fluorite type lattice. Pure ceria exhibited prominent peaks at 462 and 464 cm^{-1} for 773 and 1073 K calcined samples, respectively, which are due to the F_{2g} mode of the cubic fluorite structure.^{23,30,31} No other features existed in the spectra indicating no defects in the CeO_2 crystal lattice. The shift in the peak positions, in the case of CH and CZ samples, to higher wave numbers signifies changes in bond energies as a consequence of bond lengths as evidenced by lattice parameter estimations. Doping of lighter atoms such as Hf and Zr and subsequent contraction of the ceria unit cell may induce an increase in the F_{2g} band position. In line with XRD results, no Raman features pertaining to HfO_2 and ZrO_2 were noted. As can be observed from Figure 2, the Raman spectra are broad, which could be attributed to the reduction of phonon lifetime in the nanocrystalline regime.^{32–35} This observation also gives a clue for predicting changes in the grain size and morphology of the prepared samples.³⁶ The broadband at $\sim 620\text{ cm}^{-1}$ corresponds to the nondegenerate Longitudinal Optical (LO) mode of ceria,^{32–37} arising due to relaxation of symmetry rules which is again linked to oxygen vacancies in the ceria lattice.^{38–41} This is ascribed to a localized substitution defect vibration.⁴² The weak bands observed at around 305 cm^{-1} could be attributed to displacement of oxygen atoms from their ideal fluorite lattice positions.⁴³ The above observations also predict the possibility of the existence of a t'' phase in the mixed oxide systems.^{42,44} With increasing calcination temperature from 773 to 1073 K, in both cases, the main Raman band is sharpened with a small shift. This is due to better crystallization of the samples at higher calcination temperatures in line with XRD results.²³

XPS was employed to investigate the oxidation state of Ce in the mixed oxides. The Ce 3d core level peak of ceria is known to be complicated by the hybridization of the O 2p valence band with the Ce 4f level.^{45,46} This includes several final states for the Ce emission which are seen in the spectra. In the case of two possible cerium oxidation states (3+ and 4+) as many as

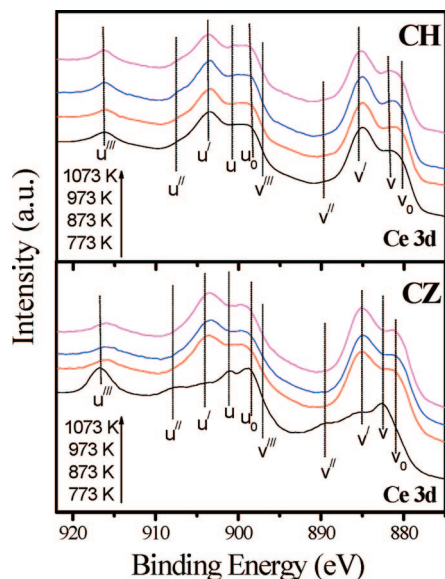


Figure 3. Ce 3d XPS spectra of $\text{Ce}_x\text{Hf}_{1-x}\text{O}_2$ (CH) and $\text{Ce}_x\text{Zr}_{1-x}\text{O}_2$ (CZ) samples calcined at different temperatures.

10 different features could be found in the Ce 3d region. The interpretation is performed by the following notations used previously,²³ and the assignment of the features in the spectra can be seen in Figure 3. Peaks labeled as “v” correspond to Ce 3d_{5/2} contributions and those labeled as “u” represent the Ce 3d_{3/2} contributions. The bands u_0 and u are the main Ce 3d_{3/2} lines, and the bands v_0 and v are the main Ce 3d_{5/2} lines of Ce^{3+} and Ce^{4+} , respectively. The band labeled as v' is a satellite to the Ce^{3+} 3d_{5/2} main line v_0 , whereas v'' and v''' are related to Ce^{4+} (main line v). Analogous assignments are valid for the corresponding “u” features. The relative intensity of the u''' feature, which is well separated from the remaining signals, is often used to assess the reduction degree of the Ce ions in the surface region. It should be kept in mind that partial reduction of cerium–zirconium mixed oxides can occur during XPS measurements. This has been noticed by many authors^{47,48} and must be taken into account when discussing quantitatively the oxidation states of surface species of the samples. Besides the X-ray dose, several factors may lead to such partial reduction like secondary electrons from the X-ray source, sample charging, temperature, vacuum, etc.⁴⁹ In the present study, the peaks at about 898.5 and 880.7 eV are the principal binding energies of Ce 3d_{3/2} and Ce 3d_{5/2}, respectively. This is significantly lower than the values typical for Ce^{4+} (900.2–900.6 and 881.7–882.0 eV, respectively),⁵⁰ which suggests a significant concentration of Ce^{3+} ions in the surface region. This is supported by the low intensity of the u''' feature in all samples except CZ after calcination at 773 K. Obviously, the surface region of our samples was strongly reduced, with the ceria present predominantly in the 3+ state, only in the surface region of CZ after calcination at 773 K were Ce^{3+} and Ce^{4+} present in comparable concentrations. The position of the primary O 1s feature (ca. 530.3 eV) is attributed to the lattice oxygen associated with the CH and CZ metal oxides. When only one peak is observed for CZ samples, one very small additional peak along with the main peak is present in CH samples (Figure 4). The peak at about 530.3 eV shown in the figure corresponds to O 1s, while the small peak at about 532.6 eV may be attributed to the adsorbed oxygen (possibly from absorbed water and/or carbonates).⁵¹ The features at about 17.2 and 18.6 eV shown in Figure 5 for CH samples are representative of Hf 4f_{7/2} and Hf 4f_{5/2}, respectively. The difference of about 1.4 eV in the binding energies between

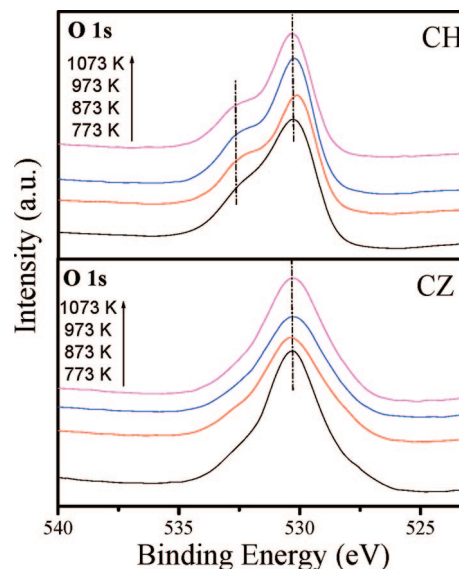


Figure 4. O 1s XPS spectra of $\text{Ce}_x\text{Hf}_{1-x}\text{O}_2$ (CH) and $\text{Ce}_x\text{Zr}_{1-x}\text{O}_2$ (CZ) samples calcined at different temperatures.

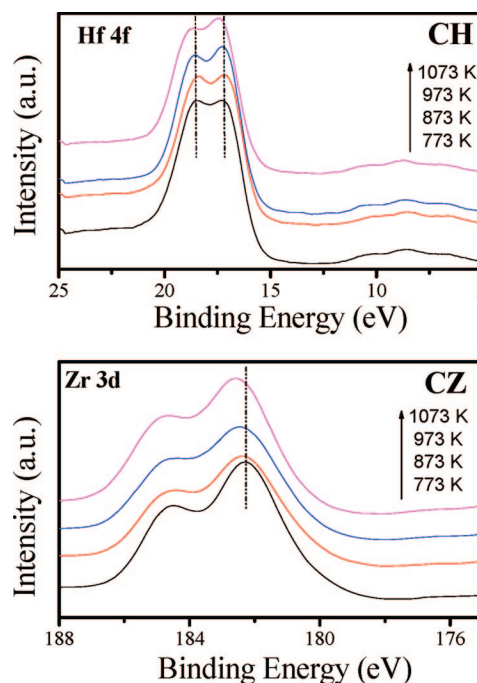


Figure 5. Hf 4f and Zr 3d XPS spectra of $\text{Ce}_x\text{Hf}_{1-x}\text{O}_2$ (CH) and $\text{Ce}_x\text{Zr}_{1-x}\text{O}_2$ (CZ) samples, respectively, calcined at different temperatures.

the Hf 4f_{7/2} and Hf 4f_{5/2} is in line with the reported values.⁵² The overlapping peaks at about 182.2 and 184.6 eV shown in Figure 5 for CZ samples correspond to Zr 3d_{5/2} and Zr 3d_{3/2}, respectively. The difference in the binding energies between the Zr 3d_{5/2} and Zr 3d_{3/2} photoemission feature is 2.4 eV, which is in agreement with the literature.^{51,52}

To examine the surface structure of the mixed oxides, ISS measurements were carried out as ISS allows the analysis of the extreme periphery of the powder particles. The intensity (cps) versus kinetic energy (eV) plots of the CH and CZ samples (773 K calcined) after definite scans are presented in Figures 6 and 7, respectively. The insets show the development of the intensity ratios between Hf and Ce, and Zr and Ce, respectively. The shifts of the signal positions in Figure 6 and to a smaller extent in Figure 7 are due to instability of the kinetic energy scale, i.e., an instrumental problem encountered in heavy-ion

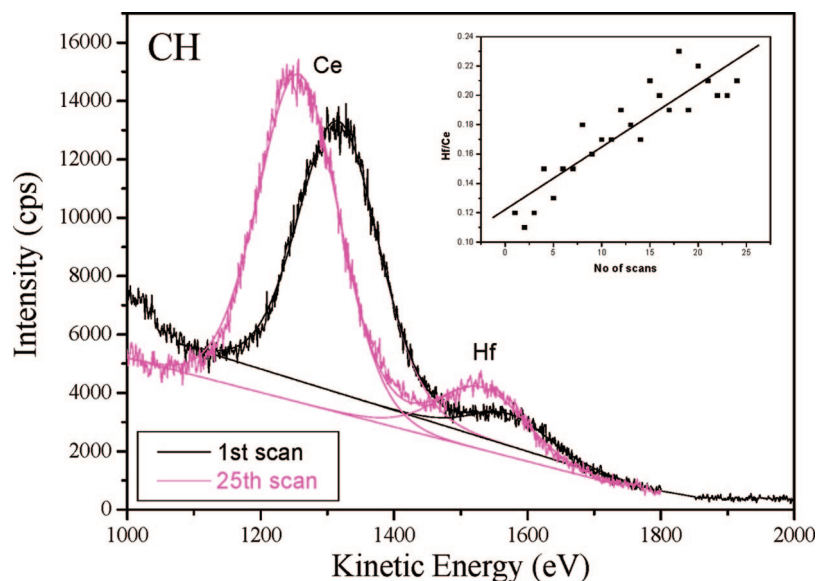


Figure 6. ISS pattern of $\text{Ce}_x\text{Hf}_{1-x}\text{O}_2$ (CH) sample calcined at 773 K after the 1st and 25th scans (inset: Hf/Ce versus no. of scans plot).

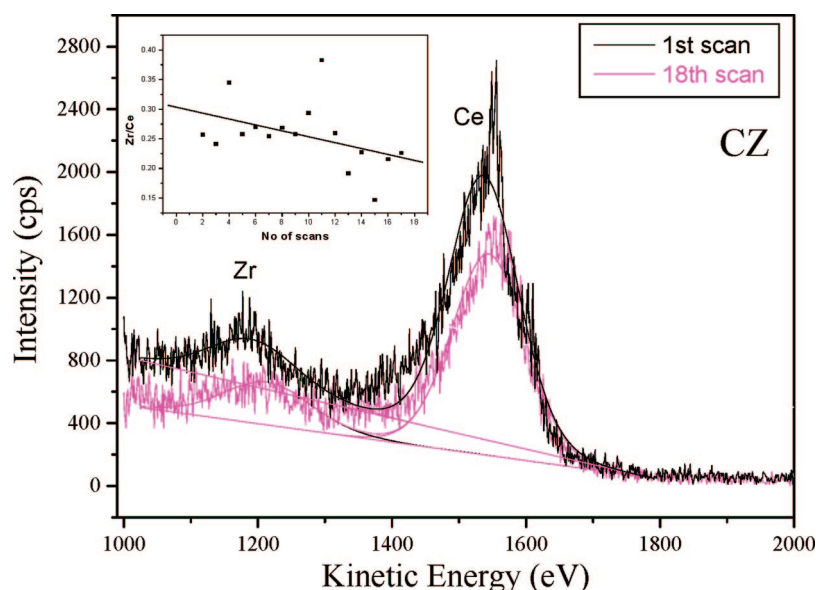


Figure 7. ISS pattern of $\text{Ce}_x\text{Zr}_{1-x}\text{O}_2$ (CZ) sample calcined at 773 K after the 1st and 18th scans (inset: Zr/Ce versus no. of scans plot).

ISS with the spectrometer used. It can be observed from Figure 6 that there is a linear increase in the Hf/Ce intensity ratio during the sputter series, i.e., the Ce is enriched at the external surface of the mixed oxide. In the CZ sample, a strong surface enrichment cannot be detected. There is a slight decrease of the Zr/Ce intensity ratio during the sputter series, but the trend is hardly significant given the rather large scatter of the experimental data. The slight surface enrichment of cerium in the CH sample, which is responsible for showing the reducible property, is expected to facilitate easy reducibility of the mixed oxide at lower temperatures. Accordingly, one can expect better activity for the CH sample compared to that of the CZ sample, which is indeed true as presented in the latter paragraphs.

Despite the difficulties in interpreting the large bandwidths and specular reflectance often observed, UV-vis DRS has been used to study various metal oxides to obtain information on surface coordination and different oxidation states of the metal ions by measuring d-d, f-d transitions and oxygen-metal ion charge transfer bands.⁵³ It is reported that the wavelength corresponding to the UV absorption edge of a semiconductive

powder such as CeO_2 can be safely used to probe the presence of nanocrystallites (<5 nm), which cannot be detected by XRD.⁵⁴ Pure CeO_2 exhibits three absorption maxima centered at ~ 255 , 285, and 340 nm in its DR spectra. The latter two absorption maxima are ascribed to $\text{Ce}^{4+} \leftarrow \text{O}^{2-}$ charge transfer and interband transitions, respectively.⁵⁵ The poorly resolved former maxima correspond to $\text{Ce}^{3+} \leftarrow \text{O}^{2-}$ charge transfer transitions.⁵⁴ As revealed by Figure 8, there are slight shifts toward higher wavelengths in the absorption edges of CH and CZ samples. Substitution of Hf^{4+} or Zr^{4+} into the CeO_2 lattice leads to lowering of symmetry and consequent strain development at the cerium sites. This may cause the observed shift toward higher wavelengths.²³ The absorption bands, which correspond to different charge transfer transitions, are poorly resolved in CZ, while the absorption edges are relatively sharp in the case of the CH sample. Moreover, the band at ~ 255 nm, which has been characterized as $\text{Ce}^{3+} \leftarrow \text{O}^{2-}$ charge transfer transition, is well resolved in CH compared to CZ samples with a slight blue-shift toward lower wavelength. The occurrence of oxygen vacancy defects as noticed from Raman spectroscopy

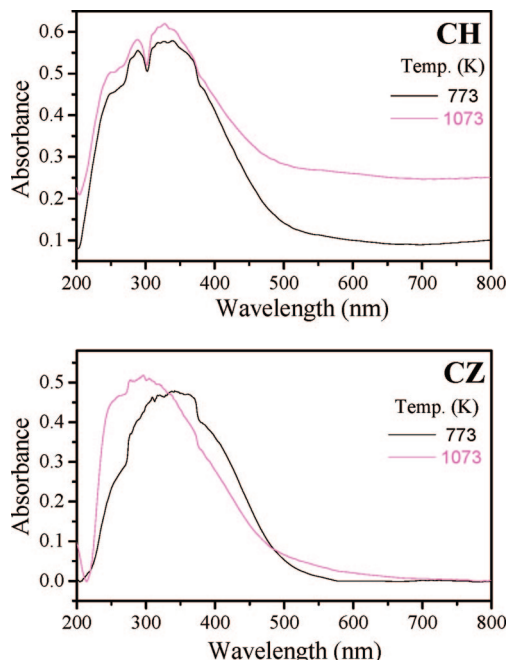


Figure 8. UV-vis DRS spectra of $\text{Ce}_x\text{Hf}_{1-x}\text{O}_2$ (CH) and $\text{Ce}_x\text{Zr}_{1-x}\text{O}_2$ (CZ) samples calcined at 773 and 1073 K.

studies supports the $\text{Ce}^{3+} \leftarrow \text{O}^{2-}$ transitions, which is more prominent in the CH sample. There is no evidence for the presence of different phases like ZrO_2 or HfO_2 from the DRS study in agreement with XRD and Raman measurements.

The general morphologies and microstructures of the CH and CZ samples calcined at different temperatures were investigated by TEM and the representative images are shown in Figures 9 and 10, respectively. The TEM images revealed nanometer-sized particles and most of them are uniform in size. The average particle sizes observed from the TEM images of the 773 K calcined samples were about 5 nm and in fair agreement with the calculated values from XRD technique. A gradual increase in the crystallite size after heat treatment at 1073 K is evident from the micrographs. The grain size increased from ~ 5 to ~ 10 nm for the CH sample and from ~ 5 to ~ 8 nm for the CZ sample with increasing treatment temperature from 773 to 1073 K, respectively. These results differ slightly with crystallite size data obtained from XRD with use of the Scherrer equation (Table 1). It should be remembered that the particle size estimations of solid solutions are subject to uncertainties due to compositional nonuniformity. Because, while using the Scherrer equation, one assumes that the particle size effects are the only source of peak broadening. A distribution of different zirconium or hafnium concentrations within individual particles as well as between particles would lead to a distribution of two- θ values and thus broader peaks which would be interpreted as reduced particles with use of the Scherrer equation.^{26,27} In both type of samples, the crystals generally formed into aggregates in which crystals not completely overlapped by others were quite rare. However, the micrographs, on the whole, represent the cubic structure of the as-prepared and high temperature calcined samples.

The OSC property was tested by oxygen release characteristics of both the samples calcined at different temperatures under dry air atmosphere in the temperature range of 573–1073 K. The change of weight of the sample was monitored by a thermogravimetry (TG) method under cyclic heat treatments in flowing air. As presented in Table 1, OSC of CH samples calcined at 773 and 1073 K are slightly greater than those of the respective CZ samples.

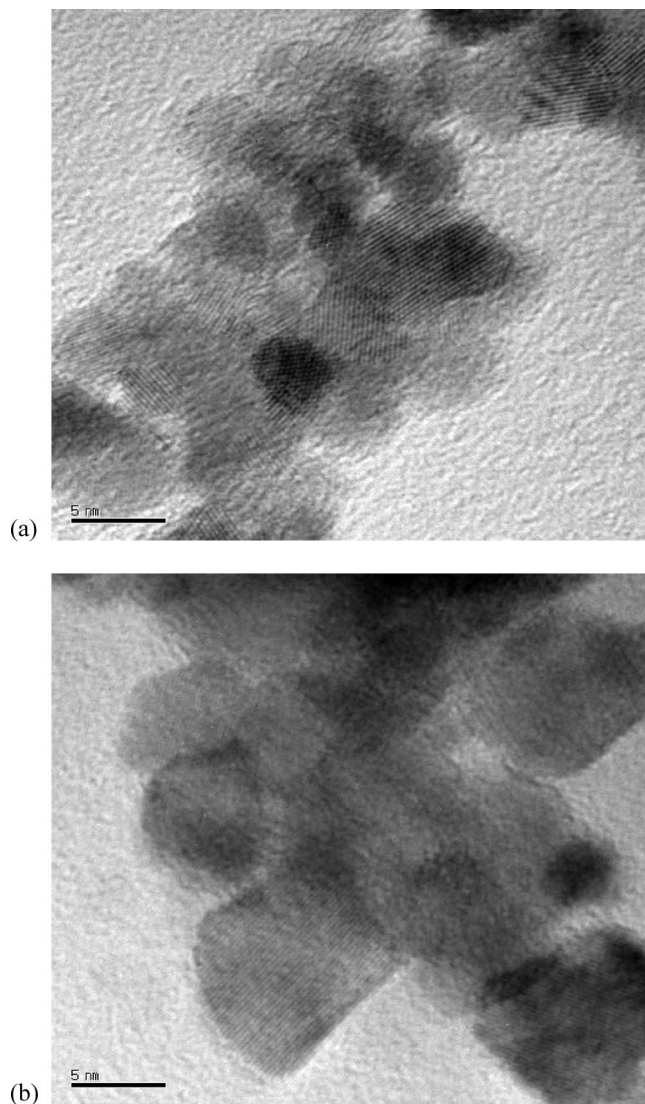
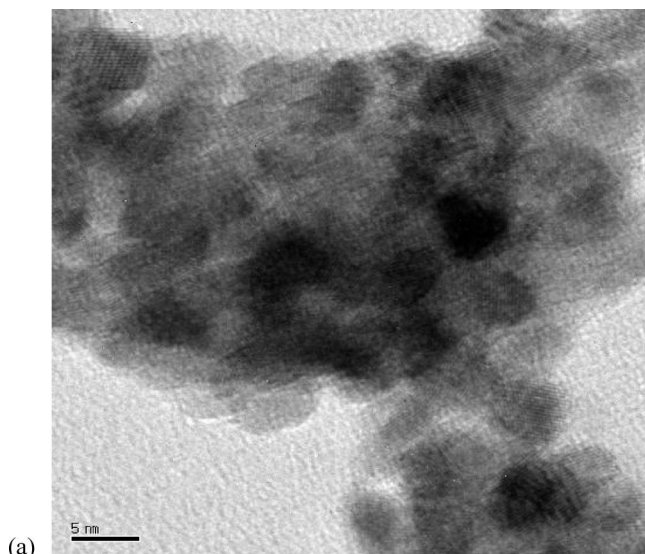
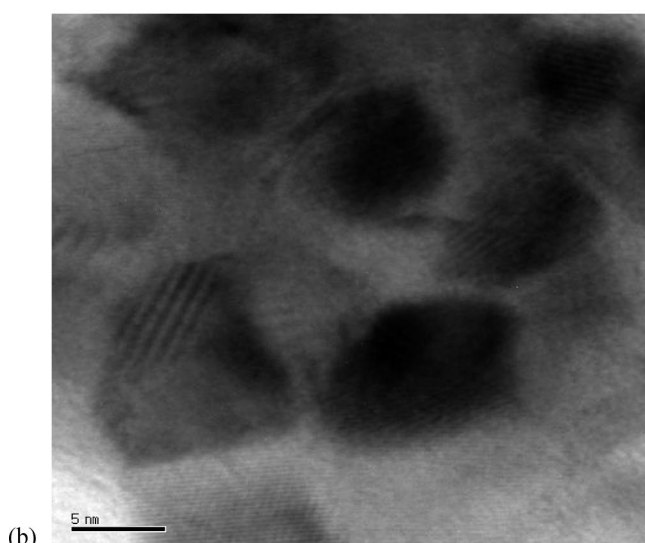


Figure 9. TEM images of the $\text{Ce}_x\text{Hf}_{1-x}\text{O}_2$ (CH) samples calcined at (a) 773 and (b) 1073 K.

This is an interesting observation from the practical viewpoint as OSC is a crucial parameter for many technological applications. The OSC of ceria-based solid solutions depends on several factors, such as surface area, particle size, method of preparation, and nature of dopants. The influence of these factors is not yet completely understood. In the present investigation the lowering of OSC values after 1073 K treatment is due to loss of specific surface area owing to agglomeration of the mixed oxides at higher temperatures. The process of oxygen-vacancy formation is closely related to the quantum effect of localization/delocalization of the 4f electron of cerium, which is the basis for the oxygen storage capacity of the cerium oxide.⁵⁶ Under reduction conditions, oxygen leaves the surface and vacant sites are formed. This process is facilitated by a simultaneous condensation of two electrons into localized f-level traps on two cerium atoms. When an oxygen atom moves diffusively toward the surface or oxygen vacancy moves, these electrons localize on cerium atoms in the immediate surrounding of the vacancy, and correspondingly, they delocalize and transfer to oxygen from Ce sites when the vacancy leaves. Thus, the formation of reduced oxides is a combined process of formation, migration, and ordering of virtual Ce^{3+} -vacancy complexes. When the external conditions change from oxygen poor to oxygen rich, this process behaves reversibly. This makes the oxygen storage-



(a)



(b)

Figure 10. TEM images of the $\text{Ce}_x\text{Zr}_{1-x}\text{O}_2$ (CZ) samples calcined at (a) 773 and (b) 1073 K.

and-release ability of ceria a remarkable property used in many modern environmentally friendly applications.⁵⁶

The catalytic activity for CO oxidation has been carried out to study the effect of isovalent cation substitution in the ceria lattice. The results at different temperatures in the range from 400 to 773 K are represented in Figure 11. As shown, the activity is enhanced by the introduction of dopant ions in the ceria lattice in the order $\text{Hf}^{4+} > \text{Zr}^{4+}$. Their OSC could be correlated with the domain size, that is, the interfacial area between CeO_2 and the constituent oxide enriched regions rather than with the surface area of the samples. Interestingly, a significant lowering of the starting reduction temperature is noticed for the CH compared to the CZ sample.²¹ The redox reactivity of ceria, especially toward CO, might strongly depend on the type and amount of surface exposed to the gas phase. The increase in CO oxidation activity for the CH sample compared to that for the CZ sample may be correlated to ISS measurement results. As mentioned, a slight surface enrichment of cerium in CH may be responsible for showing a better reducible property at lower temperatures. As a consequence one can observe light off temperature (50% conversion) at much lower value for CH compared to CZ. The OSC values of the studied catalysts could also be directly correlated to the CO oxidation activity. As can be observed from Table 1 and Figure 11, both 773 K calcined samples

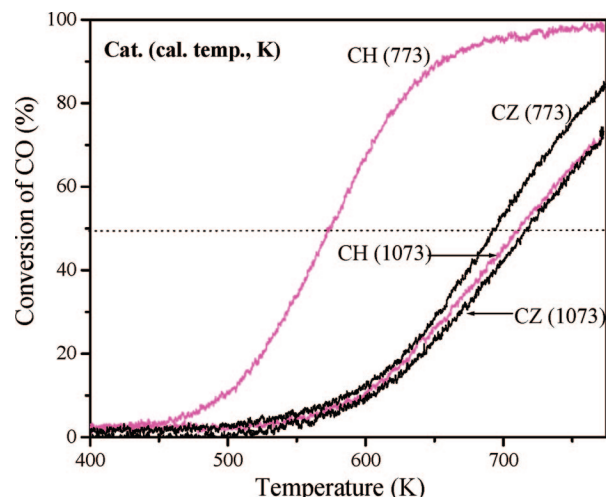


Figure 11. Conversion of CO as a function of temperature with $\text{Ce}_x\text{Hf}_{1-x}\text{O}_2$ (CH) and $\text{Ce}_x\text{Zr}_{1-x}\text{O}_2$ (CZ) samples calcined at 773 and 1073 K.

show high CO oxidation activity, CH being more efficient. After calcination at 1073 K also, the same trend is observed though the conversion efficiency was lowered due to the loss of surface area. Further, the results from Raman and UV-vis DRS studies also support the formation of oxygen vacancy and defect sites in the Ce-Hf and Ce-Zr mixed oxide crystal lattices. Especially, the presence of $\text{Ce}^{3+} \leftrightarrow \text{O}^{2-}$ transitions in the UV-vis DRS spectra (Figure 8) infers the presence of oxygen vacancy defects, which is more prominent in the case of the CH sample. These factors affect the catalytic activity of the ceria-based solid solutions, which reveals the CH sample is better for CO oxidation compared to that of the CZ sample.

In this present investigation we have studied the effect of Hf^{4+} and Zr^{4+} as dopant cations in ceria lattice as they bear comparable ionic radii (0.78 and 0.84 Å, respectively). The ease of reducibility of ceria-based mixed oxides depends on vacancy formation energy (VFE). Low VFE means high reducibility, which can lead to high OSC and improved catalytic activity. It is already reported that VFE for ceria-based mixed oxides decreases compared to ceria when smaller cations replace Ce in the lattice.⁵⁷ It is also known that VFE depends almost linearly on the ionic radius of the solute ions.⁵⁸ Apparently, in the present case, VFE for CH and CZ decrease maintaining the same trend. Moreover, one explanation is also that the presence of these smaller cations decreases the O-2p-Ce-4f band gap separation. Again, in the case of CH, phase segregation phenomenon is not observed even after the exposure of the samples to higher temperatures. Therefore, the lowering of the activity for the 1073 K calcined sample can be accounted for by loss of surface area alone. The lower reduction temperature of Ce^{4+} and thus the increased ability of CeO_2 -based mixed oxide to shift between Ce^{4+} and Ce^{3+} at a much lower temperature is the key for the increased oxidation activity. From our observations, we can come to the consensus that the difference in OSC and CO oxidation activity is not dependent on the ionicity of Hf-O or Zr-O bonds. As the ionicity of Hf-O bond is larger than that of Zr-O bonds, it is possible that the release of oxygen from the CZ sample is easier than that from CH to reduce Ce^{4+} in the corresponding mixed oxides. Interestingly, our experimental results did not follow the trend. Moreover, the formation of a pyrochlore-like structure, which may facilitate the OSC property, is hitherto unreported in the case of CH whereas the same is already reported for the ceria-zirconia system.⁵⁹ Therefore, it is thought that the ionic radii of the dopant cations have played a significant role in the observed results.

Conclusions

The structural characteristics and interdependence of the OSC and CO oxidation activity of ceria–zirconia and ceria–hafnia nanosized mixed oxides have been systematically investigated. These catalysts were synthesized by adopting a modified coprecipitation method and thermally treated up to 1073 K to study the temperature stability. The mixed oxides exhibit high specific surface area and show resistance to thermal sintering. XRD results infer the monophasic composition ($\text{Ce}_{0.75}\text{Zr}_{0.25}\text{O}_2$) for CH even up to 1073 K, while phase segregation into $\text{Ce}_{0.75}\text{Zr}_{0.25}\text{O}_2$ and $\text{Ce}_{0.6}\text{Zr}_{0.4}\text{O}_2$ was noted for the CZ sample at 1073 K. Raman spectroscopy measurements revealed the changes in the grain size and morphology of the catalyst, and defective fluorite structure leading to oxygen vacancy formation. The XPS measurements revealed the presence of both Ce^{3+} and Ce^{4+} states, which are sensitive to calcination temperature and the nature of the mixed oxide. ISS studies indicated surface enrichment of cerium in the case of the CH sample, which might be responsible for the observed better reducibility and catalytic activity of this sample. The lowering of symmetry and consequent strain development at the cerium sites is also revealed by UV–vis DRS measurements. The TEM images confirmed the nanometer-sized particles of the prepared catalysts with almost uniform size (~ 5 nm). A marginal increase in crystallite size (up to ~ 10 nm) after heat treatment at 1073 K is noticed. The OSC and CO oxidation results followed the order $\text{CH} > \text{CZ}$ under an identical set of experimental conditions. The better activity of CH could be due to formation of higher defect sites in its crystal lattice, higher OSC, and easy reducibility.

Acknowledgment. We thank Dr. S. Lorient, IRCE-Lyon, France, and Dr. Y. Yamada, AIST-Kansai, Japan, for providing Raman and XPS results, respectively. We also thank Dr. Sergiy Merzlikin, RUB, Germany, for his help in ISS measurements. B.M.R. thanks the Korea Federation of Science and Technology, South Korea for a visiting fellowship under the Brain Pool program. P.B. and P.S. thank CSIR, New Delhi, for the Senior Research Fellowships. Thanks are due to DST, New Delhi, and DAAD, Germany, for financial support under a bilateral collaboration program (DST-DAAD-PPP-2005).

References and Notes

- (1) Park, S. D.; Vohs, J. M.; Gorte, R. J. *Nature* **2000**, *404*, 265.
- (2) Xu, C. W.; Shen, P. K. *J. Power Sources* **2005**, *142*, 27.
- (3) Bance, P.; Brandon, N. P.; Girvan, B.; Holbeche, P.; O'Dea, S.; Steele, B. C. H. *J. Power Sources* **2004**, *131*, 86.
- (4) Chavan, S. V.; Tyagi, A. K. *Mater. Sci. Eng.* **2006**, *A 433*, 203.
- (5) Kim, T.; Vohs, J. M.; Gorte, R. J. *Ind. Eng. Chem. Res.* **2006**, *45*, 5561.
- (6) Bernal, S.; Blanco, G.; Cauqui, M. A.; Corchado, P.; Pintado, J. M.; Rodriguez-Izquierdo, J. M. *Chem. Commun.* **1997**, 1545.
- (7) Masui, T.; Ozaki, T.; Machida, K.; Adachi, G. *J. Alloys Compd.* **2000**, *303–304*, 49.
- (8) Reddy, B. M. In *Metal Oxides: Chemistry and Applications*; Fierro, J. L. G., Ed.; Taylor & Francis: New York, 2006; Chapter 8; pp 215–246.
- (9) Trovarelli, A. *Catal. Rev. Sci. Eng.* **1996**, *38*, 439.
- (10) Shinjoh, H. *J. Alloys Compd.* **2006**, *408–412*, 1061.
- (11) Sugiura, M. *Catal. Surv. Asia* **2003**, *7*, 77.
- (12) Reddy, B. M.; Khan, A.; Lakshmanan, P.; Aouine, M.; Lorient, S.; Volta, J. C. *J. Phys. Chem. B* **2005**, *109*, 3355.
- (13) Usmen, R. K.; Graham, G. W.; Watkins, W. L. H.; McCabe, R. W. *Catal. Lett.* **1995**, *30*, 53.
- (14) Sinev, M. Y.; Graham, G. W.; Haach, L. P.; Shelef, M. *J. Mater. Res.* **1996**, *11*, 1960.
- (15) Ozawa, M.; Matuda, K.; Suzuki, S. *J. Alloys Compd.* **2000**, *303–304*, 56.
- (16) Garcia, M. F.; Arias, M. A.; Juez, A. I.; Belver, C.; Hungria, A. B.; Conesa, J. C.; Soria, J. J. *Catal.* **2000**, *194*, 385.
- (17) Balducci, G.; Islam, M. S.; Kaspar, J.; Fornasiero, P.; Graziani, M. *Chem. Mater.* **2000**, *12*, 677.

- (18) Bernal, S.; Blanco, G.; Cifredo, G. A.; Delgado, J. J.; Finol, D.; Gatica, J. M.; Rodriguez-Izquierdo, J. M.; Vidal, H. *Chem. Mater.* **2002**, *14*, 844.
- (19) Wang, X.; Hanson, J. C.; Liu, G.; Rodriguez, J. A.; Juez, A. I.; Garcia, M. F. *J. Chem. Phys.* **2004**, *120*, 5434.
- (20) Rodriguez, J. A.; Hanson, J. C.; Kim, J.-Y.; Liu, G.; Juez, A. I.; Garcia, M. F. *J. Phys. Chem. B* **2003**, *107*, 3535.
- (21) Reddy, B. M.; Bharali, P.; Saikia, P.; Khan, A.; Lorient, S.; Muhler, M.; Grünert, W. *J. Phys. Chem. C* **2007**, *111*, 1878, and references cited therein.
- (22) Reddy, B. M.; Lakshmanan, P.; Bharali, P.; Saikia, P.; Thirumurthulu, G.; Muhler, M.; Grünert, W. *J. Phys. Chem. C* **2007**, *111*, 10478.
- (23) Reddy, B. M.; Khan, A. *Catal. Surv. Asia* **2005**, *9*, 155.
- (24) Monte, R. D.; Kaspar, J. *J. Mater. Chem.* **2005**, *15*, 633.
- (25) Bernal, S.; Kaspar, J.; Trovarelli, A. Recent Progress in Catalysis by Ceria and Related Compounds. *Catal. Today* **1999**, *50*, 173.
- (26) Reddy, B. M.; Khan, A.; Yamada, Y.; Kobayashi, T.; Lorient, S.; Volta, J. C. *Langmuir* **2003**, *19*, 3025.
- (27) Kenevey, K.; Valdivieso, F.; Soustelle, M.; Pijolat, M. *Appl. Catal. B: Environ.* **2001**, *29*, 93.
- (28) Yashima, M.; Morimoto, K.; Ishizawa, N.; Yoshimura, M. *J. Am. Ceram. Soc.* **1993**, *76*, 1745.
- (29) Kaspar, J.; Fornasiero, P.; Balducci, G.; Monte, R. D.; Hickey, N.; Sergio, V. *Inorg. Chim. Acta* **2003**, *349*, 217.
- (30) Arias, A. M.; Garcia, M. F.; Salamanca, L. N.; Valenzuela, R. X.; Conesa, J. C.; Soria, J. J. *J. Phys. Chem. B* **2000**, *104*, 4038.
- (31) Shyu, J. Z.; Weber, W. H.; Gandhi, H. S. *J. Phys. Chem.* **1988**, *92*, 4964.
- (32) Weber, W. H.; Hass, K. C.; McBride, J. R. *Phys. Rev. B* **1993**, *48*, 178.
- (33) Parayanthal, P.; Pollak, F. H. *Phys. Rev. Lett.* **1984**, *52*, 1822.
- (34) Richter, H.; Wang, Z. P.; Ley, L. *Solid State Commun.* **1981**, *39*, 625.
- (35) Fujii, M.; Hayashi, S.; Yamamoto, K. *Appl. Phys. Lett.* **1990**, *57*, 2692.
- (36) Spanier, J. E.; Robinson, R. D.; Zhang, F.; Chan, S.-W.; Herman, I. P. *Phys. Rev. B* **2001**, *64*, 245407.
- (37) Lin, X.-M.; Li, L.-P.; Li, G.-S.; Su, W.-H. *Mater. Chem. Phys.* **2001**, *69*, 236.
- (38) Reddy, B. M.; Lakshmanan, P.; Khan, A.; Lorient, S.; Cartes, C. L.; Rojas, T. C.; Fernandez, A. *J. Phys. Chem. B* **2005**, *109*, 13545.
- (39) McBride, J. R.; Hass, K. C.; Poindexter, B. D.; Weber, W. H. *J. Appl. Phys.* **1994**, *76*, 2435.
- (40) Garcia, M. F.; Wang, X.; Belver, C.; Juez, A. I.; Hanson, J. C.; Rodriguez, J. A. *Chem. Mater.* **2005**, *17*, 4181.
- (41) Hungria, A. B.; Arias, A. M.; Garcia, M. F.; Juez, A. I.; Ruiz, G. A.; Calvino, J. J.; Conesa, J. C.; Soria, J. J. *Chem. Mater.* **2003**, *15*, 4309.
- (42) Yashima, M.; Arashi, H.; Kakihana, M.; Yoshimura, M. *J. Am. Ceram. Soc.* **1994**, *77*, 1067.
- (43) Escribano, V. S.; Lopez, E. F.; Panizza, M.; Resini, C.; Amores, J. M. G.; Busca, G. *Solid State Sci.* **2003**, *5*, 1369.
- (44) Vlaic, G.; Fornasiero, P.; Geremia, S.; Kaspar, J.; Graziani, M. *J. Catal.* **1997**, *168*, 386.
- (45) Normand, F. L.; Fallah, J. E.; Hilaire, L.; Legare, P.; Kotani, A.; Parlebas, J. C. *Solid State Commun.* **1989**, *71*, 885.
- (46) Mullins, D. R.; Overbury, S. H.; Huntley, D. R. *Surf. Sci.* **1997**, *409*, 307.
- (47) Hughes, A. E.; Gorman, J. D.; Patterson, P. J. K.; Carter, R. *Surf. Interface Anal.* **1996**, *24*, 634.
- (48) Bak, K.; Hilaire, L. *Appl. Surf. Sci.* **1995**, *70/71*, 191.
- (49) Hilaire, L.; Romeo, M.; Fallah, J. E.; Normand, F. L. *J. Electron Spectrosc. Relat. Phenom.* **1995**, *73*, 89.
- (50) Nelson, A. E.; Schulz, K. H. *Appl. Surf. Sci.* **2003**, *210*, 206.
- (51) Wang, S.-P.; Zheng, X.-C.; Wang, X.-Y.; Wang, X.-R.; Zhang, S.-M.; Yu, L.-H.; Huang, W.-P.; Wu, S.-H. *Catal. Lett.* **2005**, *105*, 163.
- (52) Wagner, C. D.; Riggs, W. M.; Davis, L. E.; Moulder, J. F. In *Handbook of X-ray Photoelectron Spectroscopy*; Muilenberg, G. E., Ed.; Perkin-Elmer Corporation: Eden Prairie, MN, 1978.
- (53) Weckhuysen, B. M.; Schoonheydt, R. A. *Catal. Today* **1999**, *49*, 441.
- (54) Bensalem, A.; Verduraz, F. B.; Delamar, M.; Bugli, G. *Appl. Catal.* **1995**, *121*, 81.
- (55) Bensalem, A.; Muller, J. C.; Verduraz, F. B. *J. Chem. Soc., Faraday Trans.* **1992**, *88*, 153.
- (56) Skorodumova, N. V.; Simak, S. I.; Lundqvist, B. I.; Abrikosov, I. A.; Johansson, B. *Phys. Rev. Lett.* **2002**, *89*, 166601.
- (57) Andersson, D. A.; Simak, S. I.; Skorodumova, N. V.; Abrikosov, I. A.; Johansson, B. *Appl. Phys. Lett.* **2007**, *90*, 031909.
- (58) Shannon, R. D. *Acta Crystallogr., Sect. A: Cryst. Phys. Diff., Theor. Gen. Crystallogr.* **1976**, *32*, 751.
- (59) Baidya, T.; Hegde, M. S.; Gopalakrishnan, J. *J. Phys. Chem. B* **2007**, *111*, 5149.